



Joint Vp and Vs tomography of Taiwan: Implications for subduction-collision orogeny



Hsin-Hua Huang^{a,b,*}, Yih-Min Wu^b, Xiaodong Song^c, Chien-Hsin Chang^d,
Shiann-Jong Lee^a, Tao-Ming Chang^e, Hung-Hao Hsieh^e

^a Institute of Earth Sciences, Academia Sinica, Taipei 115, Taiwan

^b Department of Geosciences, National Taiwan University, Taipei 106, Taiwan

^c Department of Geology, University of Illinois, Urbana, IL 61801, USA

^d Central Weather Bureau, Taipei 100, Taiwan

^e National Center for Research on Earthquake Engineering, Taipei 106, Taiwan

ARTICLE INFO

Article history:

Received 19 August 2013

Received in revised form 7 February 2014

Accepted 9 February 2014

Available online xxxx

Editor: P. Shearer

Keywords:

travel-time tomography

joint inversion

borehole logging data

Taiwan orogeny

plate boundary

model evaluation

ABSTRACT

The Taiwan orogen sitting at the pre-rifted Eurasian margin and bracketed by two sub-orthogonal subduction systems is subject to complicated geotectonics, motivating numerous seismic tomographic studies in local and regional scale. Most of them obtained P-wave velocities (Vp), or with Vp/Vs ratio jointly, but few were for S-wave velocities (Vs). With unprecedented amount of S-wave data, in this study a new set of well-tuned Vp, Vs, and Vp/Vs models were determined by an elaborate joint-inversion scheme, integrating the data of P- and S-wave travel times, S–P times, and the borehole logging data (for near-surface correction) into one system. This allowed us to revisit the subduction-collision process in detail by comparing Vp, Vs, and Vp/Vs ratio simultaneously. With enhanced slab imaging of Philippine Sea Plate (PSP) under northeast Taiwan, we are able to discriminate the plausible missing Luzon forearc basement along the plate boundary and propose a “skateboarding” edge model, in which the westernmost PSP rides on the east-subducted forearc basement and subducts northward underneath the Eurasian lithosphere. The underlain forearc basement along with the PSP subduction then results in the anomalous shallow double seismic zone observed only near Taiwan Island. Meanwhile, at around 121°E the north-subducting PSP seems dipping west to collide with the deep Eurasian lithosphere, shaping an irregular corner wedge structure. In addition, we evaluate our model with previous ones by waveform modeling approach and show the current performance of travel-time tomography in Taiwan region.

© 2014 Elsevier B.V. All rights reserved.

1. Introduction

The Taiwan orogen created by the oblique arc-continent collision between the Eurasian plate (EP) and the Philippine Sea plate (PSP) is situated at the junction of two trenches with opposite subduction polarities (Fig. 1). To the east the Ryukyu trench is where the PSP subducts northward beneath the EP while to the south the South China Sea plate (SCSP), a marginal oceanic subplate of EP, subducts eastward beneath the PSP at the Manila trench. The orogeny believed started since ca. 4–6 Ma (Suppe, 1984; Teng, 1990; Liu et al., 2001) and is currently very active with a convergence rate about 80 mm/yr in a direction of N54°W (Yu et al., 1997). Owing to this high rate and the junction location between two subductions, the tectonic activities in Taiwan region is

vigorous, resulting in numerous active faults, rapid crustal deformation (Yu et al., 1997), and abundant seismicity (Wu et al., 2008) with frequent large earthquakes, e.g. 1999 M_w 7.6 Chi-Chi, Taiwan earthquake (Shin and Teng, 2001; Lee et al., 2006). Understanding such an active and complicated orogeny, gaining the knowledge of the subsurface structures is crucial.

Seismic tomography technique has played a critical role in probing the Earth structures and providing a base of tectonic exploration. With growing stations and records of Taiwan region, it has been a number of tomographic studies conducted in past decades (Roecker et al., 1987; Rau and Wu, 1995; Ma et al., 1996; Kim et al., 2005; Wang et al., 2006, 2009; Wu et al., 2007, 2009a; Kuo-Chen et al., 2012a). Roecker et al. (1987) first evidenced the subducting slabs of both the PSP and the EP south of 23°N with high and low velocity dipping zones, respectively, and the low velocity feature of the latter lent a suspicion of continental subduction (i.e. EP). The thickened crust with deep, up-arching Moho shape under the mountain region was observed later, leading

* Corresponding author. Tel.: +886 2 2783 9910x502; fax: +886 2 2783 9871.

E-mail address: hhhuang@earth.sinica.edu.tw (H.-H. Huang).

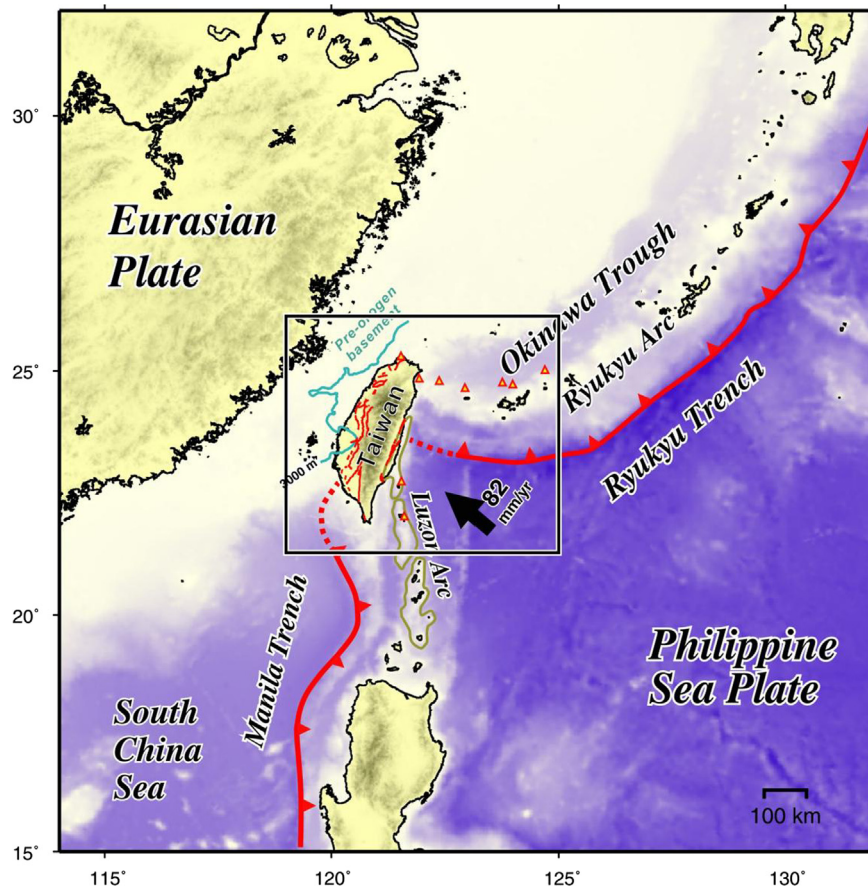


Fig. 1. Regional tectonic map for the Taiwan orogeny. The Taiwan orogen locates at the passive continental margin between the Eurasian Plate (EP) and the Philippine Sea Plate (PSP), with the convergence rate of ca. 82 mm/yr (black arrow). To the east the PSP subducts under EP at the Ryukyu trench while to the south the South China Sea Plate (SCSP), a marginal oceanic subplate of EP, subducts under the PSP at the Manila trench. The Luzon Arc (enclosed by dark yellow lines) sitting on the PSP is approaching and colliding up in orogeny by northwest plate motion. The cyan lines and red triangles denote the 3000-meter iso-depth of the pre-orogeny basement over rifted margin (Lin et al., 2003) and the volcano front related to two subductions, respectively. (For interpretation of the references to color in this figure legend, the reader is referred to the web version of this article.)

to a proposal of lithospheric deformation (Rau and Wu, 1995; Wu et al., 1997). With incorporating the Japan stations at Ryukyu Islands and a temporal Ocean Bottom Seismometer (OBS) array southeast of Taiwan, Wu et al. (2009a, 2009b) improved the imaging of two subduction zones and showed their different characteristics. Geologists usually considered the eastward subduction of EP (dragged down by the SCSP) should have started from the northern tip of the Taiwan Island (Suppe 1981, 1984; Teng, 1990; Ustaszewski et al., 2012), but the slab-like velocity anomalies in local earthquake tomography and subduction events both vanished abruptly at north of 23°N and yielded suspicions. However, by the joint inversion of local and teleseismic data, Wang et al. (2006, 2009) and Kuo-Chen et al. (2012a) imaged an east-dipping high Vp zone that can be traced down to over 200-km depth south of ca. 23.8°N. Other approaches such as investigating the teleseismic travel-time anomalies or local refracted phases also suggested the existence of subducting slab under central Taiwan (Chen et al., 2004; Lin, 2009). Although the big picture of slabs becomes clearer to date, the details of their 3D geometry and interactions have not been fully established. In particular, how the subduction-collision morphology takes place along the plate boundary, and how the subducting PSP interacts with the Eurasian lithosphere beneath the northern Taiwan need more investigations. Moreover, most of abovementioned tomographic studies were derived either only for P-wave velocity (Vp) or with Vp/Vs ratio jointly, but few were for S-wave velocity (Vs). This, in fact, restricted the tectonic discussion of Taiwan mainly on P-wave structures in the past. A ro-

bust Vp structure should be testable in Vs as well, and the S-wave tomography that usually yields stronger anomalies than P-wave (Romanowicz, 2003) can potentially help the structure delineation. The most complete regional Vs model is probably provided by Kim et al. (2005), from almost a decade ago. Although recently Kuo-Chen et al. (2012b) determined new Vs and Vp/Vs models from TAIGER project, due to short deploying period and station distribution, their data and the resolution in northeastern Taiwan, in particular for imaging the subducting PSP, were somewhat limited. This urges a need of an up-to-date Vs model for Taiwan region. Obtaining a comparable Vs model with Vp, in the meantime, can then yield more reliable Vp/Vs model for the lithological insights (e.g. Kennett and Widiyantoro, 1998; Schutt and Humphreys, 2004; Zhang et al., 2011; Eddy et al., 2013).

To obtain reliable and resolution-comparable Vp, Vs, and Vp/Vs models is never an easy task. In an intuitive sense, we can first derive Vp and Vs models separately and then simply divide Vp by Vs for Vp/Vs model. However, the Vp/Vs ratio obtained in this way is very sensitive to the respective variations of Vp and Vs and is easy to be unstable due to different ray coverage, data quality, and inversion parameters of P- and S-wave data. In contrast, one group of researchers therefore addressed on deriving the Vp/Vs model directly by assuming the identical ray-path of P- and S-waves (Walck, 1988; Thurber and Eberhart-Phillips, 1999) or by using a kernel transformation that partitions the partial derivative of Vs into those of Vp and Vp/Vs ratio (Conder and Wiens, 2006; Roecker et al., 2006). However, the former assumption (identical

ray-path of P- and S-waves) could fail for a highly heterogeneous region like Taiwan; the latter needs to deal with the error mapping problem from the Vs kernel. And again, after obtaining the Vp and Vp/Vs models by this way, the Vs model calculated from Vp and Vp/Vs ratio models suffers similar situation as we calculate Vp/Vs ratio from Vp and Vs.

Thus, in this study we aim at providing more sophisticated Vp, Vs, and Vp/Vs models jointly, with comparable resolution and internal consistency. For which a well-tuned joint-inversion scheme was implemented to derive Vp and Vs models, as well as source parameters. Although the Vp/Vs model here is calculated afterward by Vp and Vs models, in this joint inversion system the equal amount of the P- and S-wave readings were strictly selected and an additional large dataset of S–P times was incorporated to better condition the Vp/Vs determination between two models during inversion. The merit working in this way is not only to obtain a stable Vp/Vs model through unified inversion conditions of Vp and Vs, but also able to link the source relocation more tightly with not only P-wave but S-wave data and S–P times together. We also jointly integrated the borehole logging data from Engineering Geological Database (EGDT) for Taiwan Strong Motion Instrumentation Program (TSMIP) to constrain the near-surface part of model, where the rays are usually sub-vertical and seldom crossing. In addition, a long-known telemetry delay problem in data of the Central Weather Bureau Seismic Network (CWBSN) was corrected using the reported delay-time table beforehand (Chang et al., 2012). These careful corrections and the integration of various data sets (including the largest S-wave dataset compiled so far) earns us an opportunity to reexamine and reinterpret the anatomy of the Taiwan orogen in Vp, Vs, and Vp/Vs ratio. On the other hand, the updated Vs model here, in particular with the shallow part constrained by the logging data, is also important in simulating more accurate ground motion (S-wave dominates) for the research of source modeling, engineering, and hazard mitigation. The models of this study are publicly released in the supplementary for various tests and applications.

2. Data collection and process

The densely distributed regional seismic network used in this study was combined from several permanent networks and temporal arrays (Fig. 2a), which includes: (1) CWBSN, a permanent seismic network responsible for routinely earthquake monitoring in Taiwan region (Shin 1992, 1993); (2) TSMIP, a strong-motion program which has had over 700 digital accelerographs in free field sites since 1991 to present (Shin et al., 2003); (3) The broadband seismic network combing stations operated by the Broadband Array in Taiwan for Seismology (BATS) (Kao et al., 1998) and the Central Weather Bureau (CWB); (4) JMA (Japan Meteorological Agency) seismic stations on Ryukyu arc (Wu et al., 2009a); (5) Part stations of TAIGER project, including some inland broadband stations and two linear OBS arrays western offshore (Kuo-Chen et al., 2012a); (6) The temporal OBS array deployed by Nation Central University (NCU) for the Pingtung earthquake (Liao et al., 2008); (7) Three OBSs of the Taiwan Ocean Research Institute (TORI) settled in southeast offshore; And (8) two stations in Fujian province, China (Fig. 2a). A total of 1210 stations are combined in the end, from which all the data are then collected and relocated beforehand following the process of Wu et al. (2008).

A few data criteria are further made for the tomographic inversion. First of all we only retain high quality data and exclude all the readings with picking quality higher than level 2 (level 0–4 in total and 0 is the best, referring to the CWB picking criteria). Secondly, since we include the source parameters into inversion (see details in Section 3.1), only the events at least recorded by 4 stations for both P- and S-readings with an azimuthal gap angle (GAP) <180°

are selected. That is, each event is promised to has identically more than 4 P- and 4 S-arrivals with high-quality picking (<level 2). This criterion is also very important for better conditioning the Vp/Vs model with nearly identical condition of P- and S-wave data, such as similar ray coverage and similar weight in joint inversion. To the end, there are 69,353 events, 1112 stations, and 989,995 readings of P-wave, S-wave, and S–P times being sorted out at this stage.

To further optimize the inversion problem of a sparse ill-conditioned matrix like seismic tomography. One of the approaches is to minimize the heterogeneity of the earthquake distribution as much as possible, which was also considered in the previous studies (Kim et al., 2005; Wu et al., 2007). But instead of their regular cell binning, a more sophisticated 3D source grouping method is adopted (Liang et al., 2004). This method aims at grouping earthquake clusters spatially with certain predefined radius (we chose 2 km here). It starts at selecting the first event (in the order of the event file) as sphere center to include subsequent events within the radius as the first group, then chooses another event which is not included in the first group to be the center of the second group, and keeps on grouping to the end. For an event belonging to several groups, group it into the nearest one. After grouping is applied to all events in order, the averaged locations of events in each group are used as new sphere centers to regroup the events again in the next iteration. As a result, some groups may be canceled and some new groups will be generated. This procedure will keep iterating until no groups are canceled or generated. We then pick the event with the most readings in each cluster for the inversion. This way, unlike the regular cell binning, is data-adaptive and guarantees a 3-D uniform distribution over the earthquake clusters. Ultimately, we obtained an even distribution of events than original (Fig. 2b), with a reduced number of 7587 events, 1050 stations, and 200,051 readings. The details of final sorted data contributed from respective networks and arrays can be found in the supplementary (S.1).

3. Methodology

3.1. Tomographic inversion

The benefit of including source parameters into tomographic inversion has already been confirmed both experimentally (Thurber, 1992) and mathematically (Roecker et al., 2006). Its linearized discrete form for the simultaneous inversion of the slowness and source parameters can be expressed as:

$$d = t_i^{obs} - t_i^{pred} = \sum \left(\frac{\partial t}{\partial s} \right)_i \Delta s_i + \sum \left(\frac{\partial t}{\partial h} \right)_i \Delta h_i = G \begin{bmatrix} S \\ H \end{bmatrix} \quad (1)$$

where t_i^{obs} and t_i^{pred} are the observed and predicted travel times. The d and G then represent the data vector and the kernel matrix, and S and H are model vectors for the perturbation of slowness Δs and the source parameter Δh to be sought in the inversion. The model is specified by assigning a slowness to each node in the grid; for the slowness, s , at any point is then determined via tri-linear interpolation of the s_j at the surrounding 8 nodes as:

$$s = \sum_{i=1}^8 c_i s_i \quad (2)$$

where the c_i is the interpolation coefficient that depends on the fractional distance of the point in demand from the surrounding nodes.

For multi-dataset integration, the system has a detail matrix form as

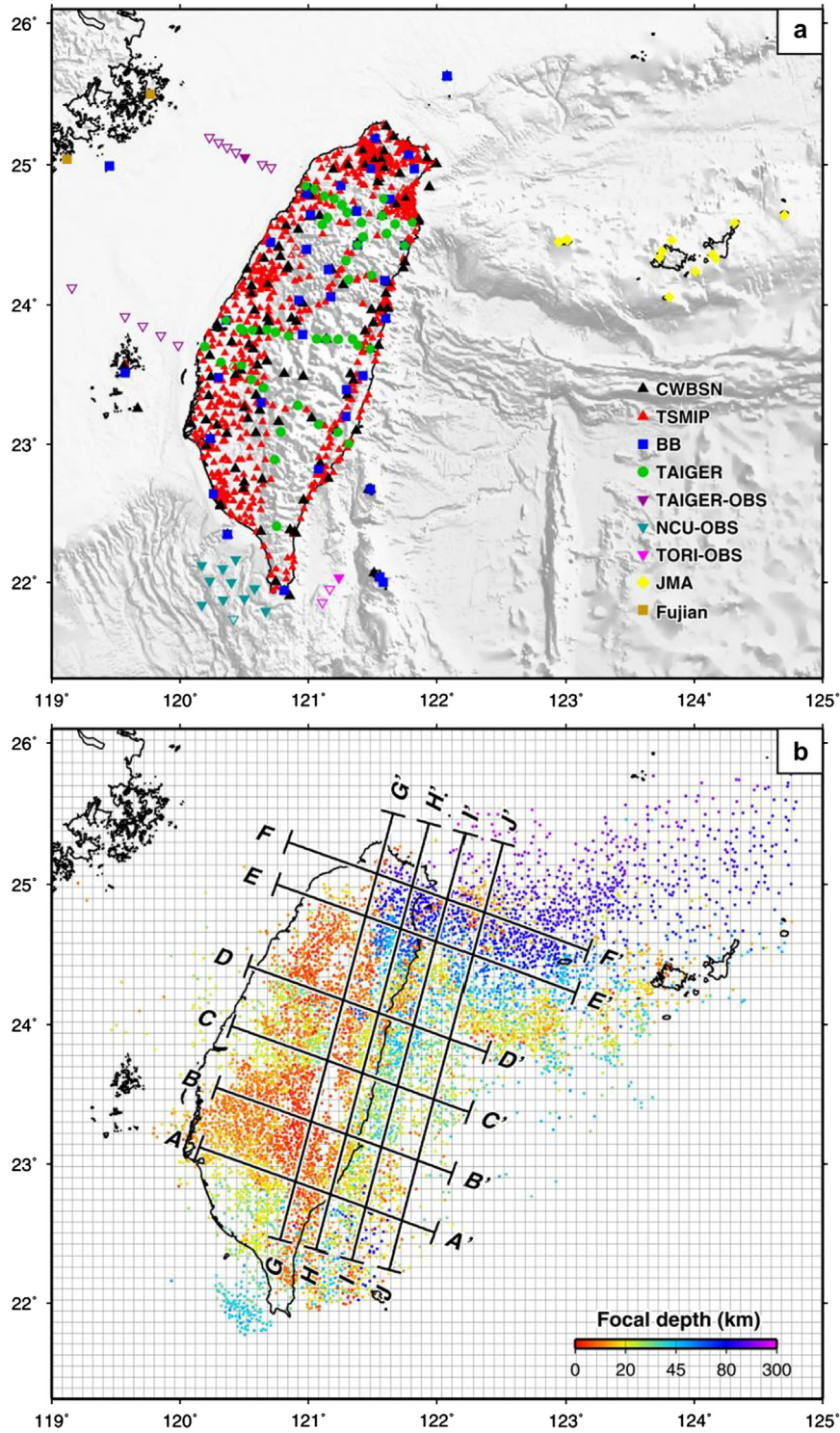


Fig. 2. (a) The station distribution of the integrated seismic network. Solid symbols represent the used stations after data sorting. CWBSN: Central Weather Bureau Seismic Network, TSMIP: Taiwan Strong Motion Instrumentation Program, BB: Broadband Array, OBS: Ocean Bottom Seismometer arrays deployed by National Central University (NCU), Taiwan Ocean Research Institute (TORI), and TAIGER (Taiwan Integrated Geodynamics Research) project (b) The distribution of the earthquakes sorted by the 3-D grouping algorithm (Liang et al., 2004). The background thin lines shows the model gridding with ca. 8 km interval, and black thick lines denote the profile locations in Fig. 6.

$$\begin{pmatrix} G_P & 0 & G_h \\ 0 & G_S & G_h \\ -G_P & G_S & G_h \\ rI_P^c & 0 & 0 \\ 0 & I_S^c & 0 \end{pmatrix} \begin{pmatrix} m_P \\ m_S \\ m_h \end{pmatrix} = \begin{pmatrix} d_P \\ d_S \\ d_{S-P} \\ C_P - M_P^c \\ C_S - M_S^c \end{pmatrix} \quad (3)$$

where the G_P and G_S are partial derivatives of travel times for P-wave and S-wave respectively; the G_h represents the partial derivatives of the source location and the origin time; and then S–P times can be accomplished by a form as $G_S - G_P$. The d_P , d_S , and d_{S-P} are the corresponding residual vectors. The m_P , m_S , and m_h are the model perturbation for the P- and S-wave velocities and source parameters we simultaneously seek.

3.2. Near-surface correction

For the problem of the poorer resolution under stations (where the ray paths are usually subvertical) it has often been considered by involving a station correction term in local tomography but seldom been constrained quantitatively. The Engineering Geological Database for TSMIP (EGDT) that measured the logging P- and S-wave velocities in shallowest 30–60 meters at 445 drilling sites over the Island provides valuable and accurate information of near-surface velocity structures for use (Kuo, C.H. et al., 2012b). However, since the depth extension of logging-measured velocity is unknown. Rather than forcing the topmost layers of model to the logging values, we implemented a joint inversion with near-surface correction as in Eq. (3), where $C_{P,S}$ denotes an a priori model (subscripts P and S represent the P-wave and S-wave model, respectively), and $M_{P,S}^c$ is then the part of model space we want to correct to $C_{P,S}$. $I_{P,S}^c$ is the corresponding unit matrix and r is a weighting to make the corrections for P- and S-wave velocity convergent in similar order (usually the Vp/Vs ratio of 1.73 is used). In this form the velocity solution between 30–60 m and 500 m of model grid will be naturally sought by best fitting both the seismic and logging data. In addition, we do not apply the smoothing regularization (Section 3.3) onto the top layers above 500 m depth. Therefore the nodes at surface and 500 m depth can afford very high velocity gradient and prevent forcing too much low velocity toward deep. Moreover, due to the drilling sites not exactly located at the model nodes, each onsite correction is achieved by adjusting the velocities at surrounding 8 nodes, which is in the form as same as we extract the slowness between nodes (Eq. (2)):

$$C - m_c = \sum_{i=1}^8 c_i s_i^{bh} - \sum_{i=1}^8 c_i s_i^{mod} \quad (4)$$

where the s_i^{mod} and s_i^{bh} are the model slowness at surrounding nodes and the borehole logging slowness we want to match. After extensive tests, we weighted the seismological dataset 1.0, and 5.0 times for the borehole logging data that are regarded as “ground truth” directly estimated onsite. Besides, we also adopted the picking quality weighting. For the CWB picking level 0–2 we used. The level 0, 1, and 2 correspond to weighting 1.0, 0.8, and 0.6, respectively.

3.3. Regularization and preconditioning

For a sparse, ill-conditioned matrix, commonly the regularization will be introduced into inversion for stability (e.g. damping and smoothing constraints) as the form:

$$\begin{pmatrix} W\tilde{G} \\ \lambda I \\ \phi L \end{pmatrix} \tilde{m} = \begin{pmatrix} W\tilde{d} \\ 0 \\ 0 \end{pmatrix} \quad (5)$$

where \tilde{G} , \tilde{m} , and \tilde{d} represent the matrix form in Eq. (3), and W is the weighting scheme we described in Section 3.2. I and L are the unit matrix and the finite-difference Laplacian operator (Lees and Crosson, 1989), in charge of the magnitude and the roughness over the model space; λ and ϕ are then their coefficients to control the respective levels, which are chosen as 30 and 20 in this study (see more detail descriptions in supplementary S.2).

Lastly, because Eq. (1) contains quantities with different units (the km/s for velocity, and the km and sec for source location and original time, respectively), a preconditioning matrix P was applied to make the kernel matrix \tilde{G} dimensionless in joint inversion (Xu and Song, 2010; Huang, H.H. et al., 2013b). P is a diagonal matrix whose diagonal elements are the reciprocal of the $L2$ norm of each column vector in kernel matrix \tilde{G} . This process makes $\tilde{G}' = \tilde{G}P$, $\tilde{m}' = P^{-1}\tilde{m}$, and does not change the linear system as $\tilde{G}'\tilde{m}' = \tilde{G}PP^{-1}\tilde{m} = \tilde{d}$. To the end, the desired model vector can then be recovered by $\tilde{m} = P\tilde{m}'$.

4. Model setup and assessment

4.1. Initial 1-D velocity model and model parameterization

Rather than conducting a 1-D inversion first to obtain the initial 1-D velocity model for 3-D inversion (Kissling et al., 1994), the initial 1-D P-wave velocity model here is directly averaged from a regional 3-D P-wave velocity model (Wu et al., 2009a). Based on the Wadati diagram of our data, we obtained a regressed Vp/Vs ratio of 1.728 and then used this value to convert the initial 1-D Vp model to the initial 1-D Vs model (Fig. 3).

The 3-D velocity model is parameterized into 76×61 horizontal nodes in 0.08° (\sim ca. 8 km) spacing (Fig. 2b), and 27 vertical nodes with the increasing interval from 0.5 to 50 km toward the depth (dots in Fig. 3) in a spherical coordination rather than the cartesian coordination in previous models (Kim et al., 2005; Wu et al., 2007, 2009a). A modified pseudo-bending method is adopted for ray-tracing in 3-D spherical medium (Um and Thurber, 1987; Koketsu and Sekine, 1998) to deal with the long-path rays more properly, e.g. the diving waves from far-offshore subduction events to the Island stations in particular. The top and bottom of the model are set at -5 and 300 km to contain the elevation of stations and the deepest earthquakes in the Ryukyu subduction zone (downward direction is defined as positive). The advantage of elevating the model top to include the station height is to make the ray tracing fully within the model space and does not require the additional travel-time correction for topography.

4.2. Model assessment

We perform a checkerboard test (Leveque et al., 1993) to assess the model resolution. The synthetic model is constructed by perturbing $\pm 5\%$ variations of 1-D initial velocities in both longitude, latitude, and depth direction. Due to opposite variation of Vp and Vs, the Vp/Vs perturbation is then therefore $\pm 10\%$. We also added both the random noise on travel times and the mislocations on hypocenters for reality. In our test, the results show a good convergence of simultaneous inversion for both velocity and source parameters (see details in supplementary S.3). Rather than only inverting the velocity variations for checkerboard test in most studies, including the mislocation term is more realistic and meaningful to us.

Afterward, we can then translate the recovery level of synthetic models into a resolvability factor, R (Zelt, 1998; Huang, B.S., et al., 2013a), which defined as

$$R = \frac{\sum_{i=i-n}^{i+n} \sum_{j=j-n}^{j+n} \sum_{k=k-1}^{k+1} (Vt_{i,j,k} + Vr_{i,j,k})^2}{\sum_{i=i-n}^{i+n} \sum_{j=j-n}^{j+n} \sum_{k=k-1}^{k+1} (Vt_{i,j,k}^2 + Vr_{i,j,k}^2)} \quad (6)$$

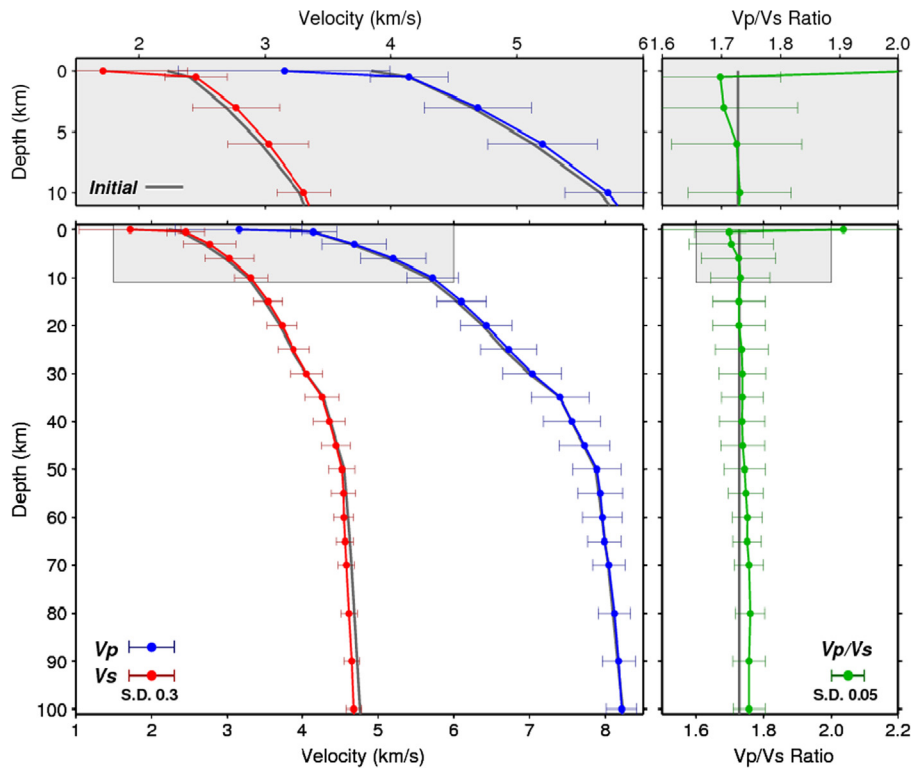


Fig. 3. Initial 1D models (dark gray lines) and averaged 1D models from 3D inverted models for P-wave (blue line) and S-wave velocity (red line), and their ratio (green line). Upper panel is the zoom-in plots of the shallow part of model (0–10 km, shaded area) in lower panel. The dots and horizontal bars denote the depths of model nodes and the standard deviations of velocity variation at that depth, respectively. (For interpretation of the references to color in this figure legend, the reader is referred to the web version of this article.)

where V_t and V_r are the true (i.e. known synthetic model) and the recovered velocity at a node denoted by indexes i, j, k in three-dimensional space. This resolvability factor will then be operated over a certain range by a desired number of nodes, n . A larger value of n produces a smoother map, and vice versa. We chose $n = 5$ in this case, which is slightly larger than the perturbation wavelength in the checkerboard test, and can usually produce the fair results. R ranges from 0 to 1, in which $R = 1$ represents the velocity anomaly is 100% recovered (nodes with well ray crossing), $R = 0.5$ means 0% recovered (nodes with no ray passing), and $R = 0$ is that the velocity is -100% perturbed (unstable inversion nodes). Compared to the recovery level of checkerboard model, $R = 0.6$ is considered a reasonable lower bound of well-resolved area in this study. R is used as an index to blank the area with the value smaller than 0.6 in tomographic images (Figs. 4, 5, and 6).

5. Results and discussion

The joint inversion was iterated until the residual reduction became insignificant (7 iterations in our case). The total root-mean-square (RMS) of data residuals is reduced significantly from 0.9 to 0.3 sec, about 67% reduction. The individual residual distribution and reduction of the P- and S-wave travel times, and S–P times are described in supplementary Section S.2 (Fig. S.3). The rest of the residuals not eliminated during the inversion may arise from the inevitable picking errors and the effect of anisotropy and discontinuity not yet considered in the model.

5.1. Averaged 1-D models and near-surface effects

The inverted 3-D models are averaged to compare with the initial 1-D models (Fig. 3). Since the initial 1-D models were also converted from a previous 3-D model (Wu et al., 2009a), basically they

are similar except the shallow part. Due to the joint inversion with logging data, the velocity structures would tend to approach the low value of logging data at near-surface (ca. 0–1 km) and cause the velocity rising in the deeper depth for compensating the travel times, resulting in a steeper velocity gradient and a more bending curve in Vp/Vs ratio at near-surface. This bending curve caused by the unconsolidated sediments or sedimentary rocks conforms to the compiled empirical relations (Brocher, 2005), and should be realistic. A recent study of Huang, B.S. et al. (2013a) also pointed out the necessity of existence of a steep velocity gradient for modeling the observations of multiple diving waves in western Taiwan coastal plain. An increase of Vp/Vs ratio around the depth of 45–50 km, on the other hand, may represent the regional average depth of Moho due to the mineral transition from felsic- to olivine-phase rocks, as shown in many models (Kennett et al., 1995; Tellez and Cordoba, 1998).

In a 3-D point of view, the effect of near-surface correction is more complicated to conclude. The most obvious difference can be seen in the tomographic images at surface, where Vp and Vs show the tremendous low values with high Vp/Vs ratio at plains and basins, as well as Longitudinal Valley (Fig. 4, uppermost panel). This is mainly constrained by the borehole logging data and hardly achieved by the ordinary tomographic inversion (see Fig. S.6 for comparison). These resultant near-surface structures potentially can facilitate the waveform simulation into higher frequency regarding to more ground-truth site effects (Lee et al., 2008). On the other hand, the near-surface correction is not only important for the shallow portion but also has the effects on calibrating some portions in the model where the data do not well constrain, e.g. deeper structures only sampled by long-path diving rays. It acts, in fact, similar to the station correction in conventional, but the difference is that rather than use additional free parameters to absorb the average travel-time residuals at stations, we constrain this term by the true ground measurements at logging sites.

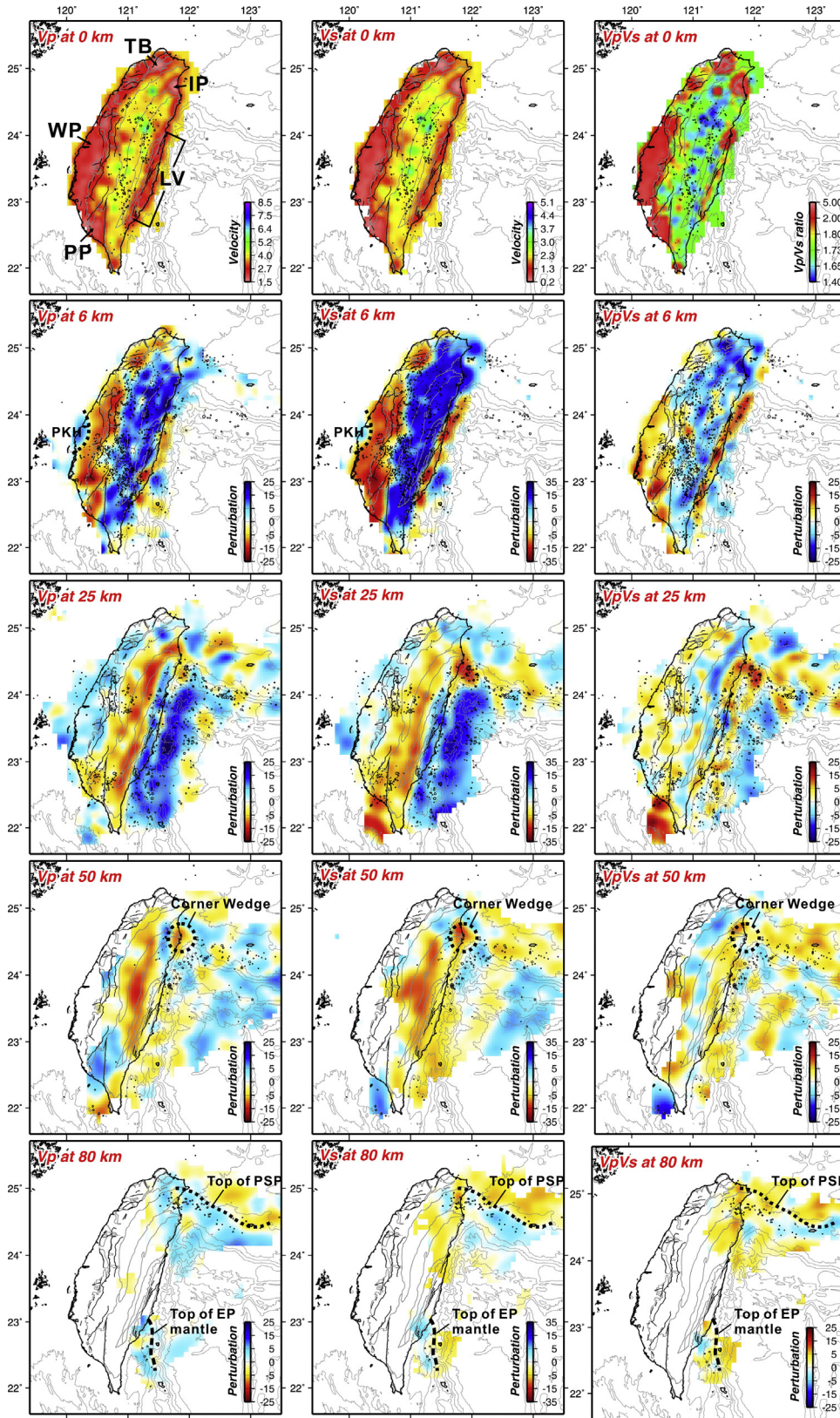


Fig. 4. Tomographic images for V_p , V_s , and V_p/V_s ratio from left to right at different depths. The uppermost panel shows the absolute values of V_p , V_s , and V_p/V_s ratio, and the others show the perturbations relative to the 1D initial models (Fig. 3). TB: Taipei Basin, IP: Ilain Plain, WP: Western Plain, PP: Pingtung Plain, LV: Longitudinal Valley. Dashed lines, and circles indicate the structures we discussed in text.

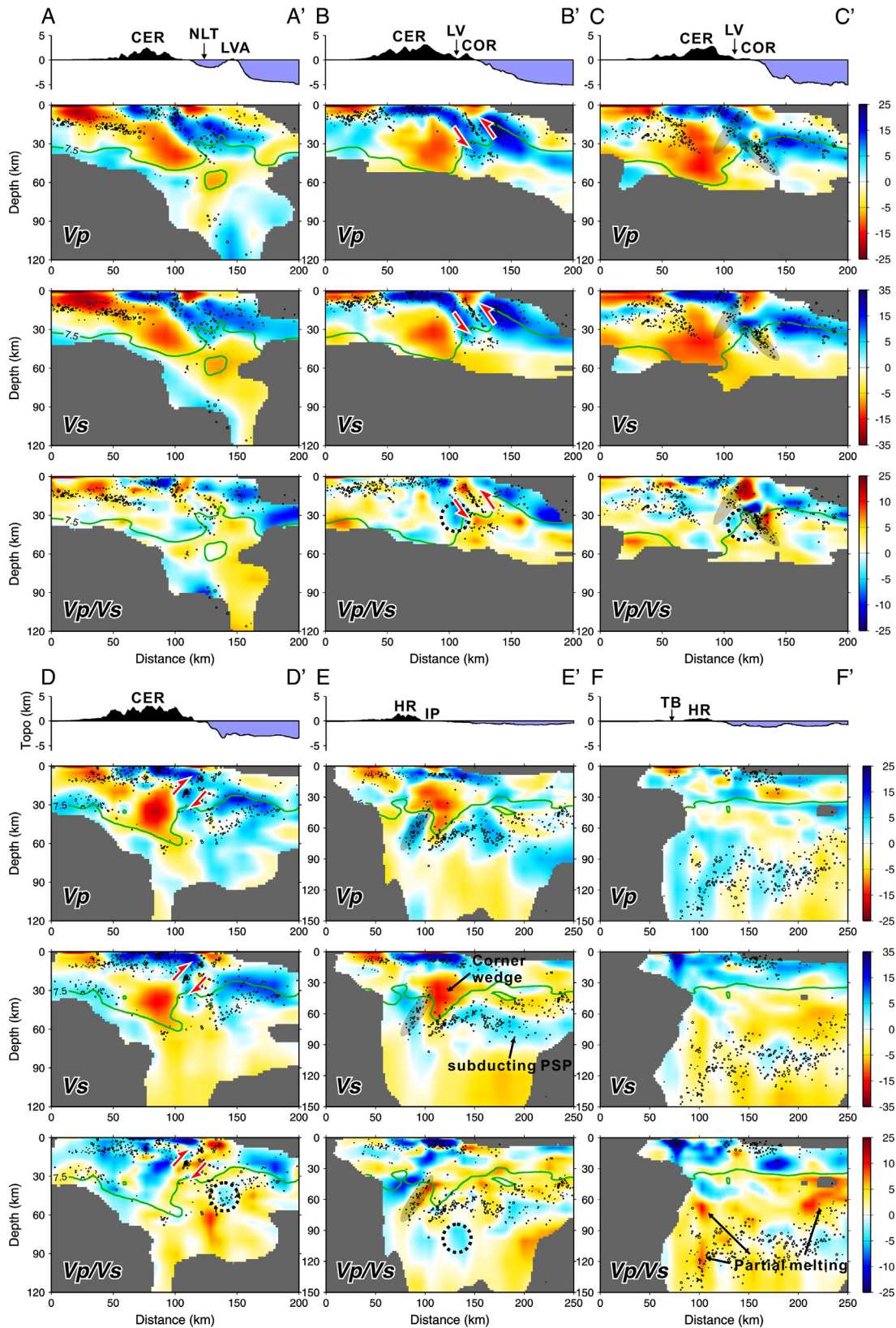


Fig. 5. EEN-WWS vertical profiles of V_p , V_s , and V_p/V_s ratio in upper, middle, and lower panels, respectively. The profile locations are shown in Fig. 2b. The iso-velocity of $V_p = 7.5$ km/s is denoted by the green line for Moho reference in first order. The red arrows indicate the faulting sense of earthquake clusters. The shaded ellipse and the dashed circle both indicate the structures we described in text. CER: Central Range, NLT: Northern Luzon Trough, LVA: Luzon volcanic arc, COR: Coastal Range, LV: Longitudinal Valley, HR: Hsuishan Range, IP: Ilan Plain, TB: Taipei basin.

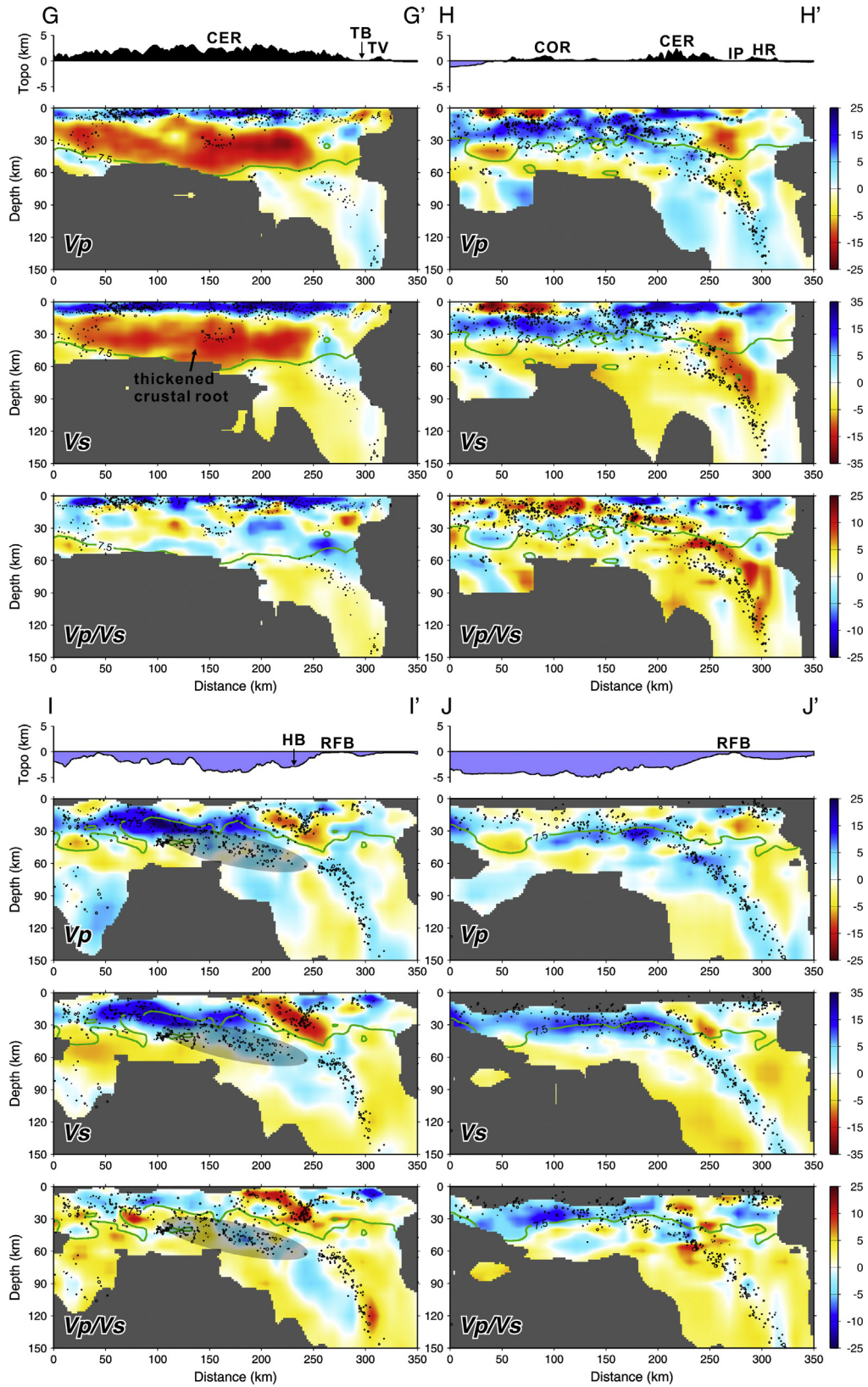


Fig. 6. NNE-SSW vertical profiles of V_p , V_s , and V_p/V_s ratio in upper, middle, and lower panels, respectively. The profile locations are shown in Fig. 2b. The iso-velocity of $V_p = 7.5$ km/s is denoted by the green line for Moho reference in first order. The shaded ellipse indicates the structures discussed in text. CER: Central Ragne, COR: Coastal Ragne, HR: Hsuishan Range, IP: Ilan Plain, TB: Taipei basin, TV: Tatun Volcano, HB, Hoping basin, RFB: Ryukyu forearc basement.

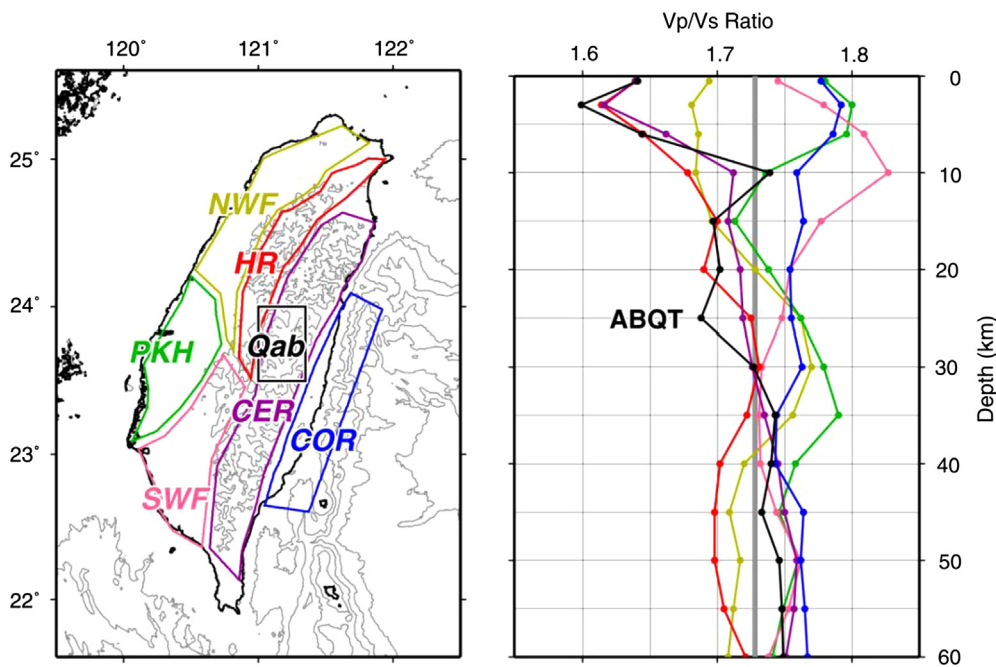


Fig. 7. Local tectonic regions of Taiwan (left) and corresponding 1D Vp/Vs models (right). NWF: Northern Western Foothill, PKH: Peikang High, SWF: Southern Western Foothill, HR: Hsuisan Range, CER: Central Range, COR: Coastal Range, Qab: the area where Kuo-Chen et al. (2012b) found the Quartz α - β transition. ABQT denotes the possible depth of Quartz α - β transition.

5.2. 3-D models and slab imaging

Fig. 4 shows the horizontal images at different depths. The main feature in the central Taiwan, Peikang High (PKH) (Lin et al., 2003), is retrieved more shallowly than previous (Wu et al., 2007), at 6 km depth in our model. This may arise from the effect of near-surface correction that increases the velocity gradient in shallow depth. Its fan shape can also be clearly delineated in both Vp and Vs down to 20 km deep, but intriguingly not observed in Vp/Vs ratio. In southwestern Taiwan, the Pingtung Plain (PP) seems to cumulate massive sediments or high-porosity rocks with low velocities and the high ratio all the way down to the 20-km depth, implying a rapid deposition environment. To the east, the Longitudinal Valley characterized by low Vp and Vs, and high Vp/Vs ratio at shallow depth may reflect the valley sediments and the volcanic rocks (Christensen and Mooney, 1995; Christensen, 1996). Down to the depth of 20 and 35 km, the high Vp and Vs clearly denote the outline of PSP to the east; and a commonly-observed velocity reversal pattern under the mountain areas is shown as well, denoting a thickened crustal root by the collision (Rau and Wu, 1995; Kim et al., 2005; Wu et al., 2007; Kuo-Chen et al., 2012a). At depth of 50 and 80 km, the subducting slabs can be readily depicted in our model. Besides, at the location around longitude 121.9°E and latitude 24.7°N (dashed circle), a noticing low-velocity anomaly that is encompassed by high velocities and seems shifted from the northern extension of the thickened crustal root under mountains is observed. We address this structure in later profiles.

In profiles (Figs. 5 and 6), comparing with the latest two models (Wu et al., 2009a and Kuo-Chen et al., 2012a), our models show the strength to imaging more sharpened and continuous subducting slab for SCSP/EP (profile AA') and for PSP (profile II' and JJ') by either high Vp or Vs, without any predefined setting (see profile comparison in Section S4.2 and Fig. S.7). This particularly benefits the tectonic interpretations in Sections 5.3 and 5.4. According to the previous study (Kuo-Chen et al., 2012a), the iso-velocity line of $V_p = 7.5$ km/s is referred to as the presumed Moho interface here for differentiating the crustal and mantle structures

in first-order. Note that although the $V_p = 7.5$ km/s is an approximation, it turns out very consistent with our Vp/Vs variations across Moho. In profile II', a conspicuous feature, characterized by low Vp, Vs, and high Vp/Vs ratio, is found atop the PSP at depth 10–40 km above Moho. It implies the occurrence of the serpentinization within upper plate (Hacker et al., 2003; Chou et al., 2009) or a subduction channel with eroded forearc debris and sediments (Cloos and Shreve, 1988). Another rather high Vp/Vs anomaly patch with mainly the decrease of Vs, at deeper depth of 120 km, indicates the partial melting process on the other hand. This plausible melting feature, westward to the profile HH', is even more obvious and seems rising up to the depth of 60 km right beneath the Ilan plain offshore (see profile FF' as well), in accordance with that Lin et al. (2004) reported. By contrast, in profile AA' the high Vp, Vs slab-like imaging of SCSP/EP that overlaid by a massive low velocity zone (~30 km thick) with moderate Vp/Vs variation shows distinct characteristics from slab imaging of PSP. Since the boundary between the high- and low-velocity east-dipping zones agrees well with the Moho interface ($V_p = 7.5$), we suggest that the high Vp, Vs slab-like imaging likely represents the mantle part of EP. Following this interpretation, it may indicate that, in southern Taiwan, the EP has been dragged down (by SCSP) and subducted, at least partly. But it is unfortunate that we lose the slab resolution northward in profiles BB' and CC' due to a lack of subduction events and offshore stations with wide spanning in this region. However, shown in the recent P-wave model of TAIGER project (Kuo-Chen et al., 2012a), this east-dipping structure of high Vp seems to be able to extend northward. Further studies examining the deep structures northward under central-to-northern Taiwan in more detail will be a critical extension of this study.

5.3. Vp/Vs structures and the missing forearc-basement

With the careful-conditioned Vp/Vs model in this study, we also investigated the Vp/Vs structures to different local tectonic regions in Taiwan (Fig. 7). Although the results show a range of diversity, the mountain regions such as Hsuisan Range (HR), Central

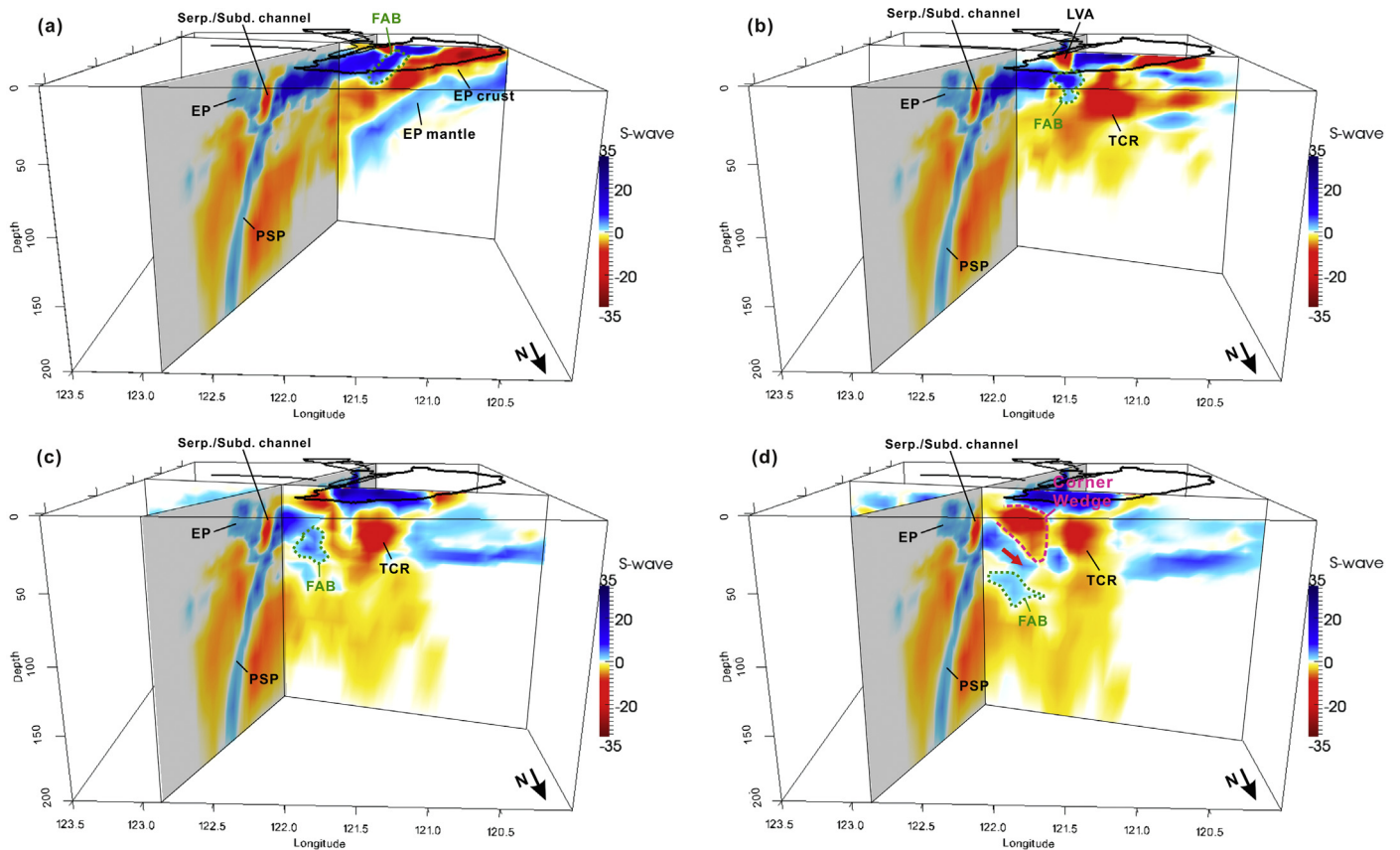


Fig. 8. The 3-D view of Vs model, displaying the subduction-collision process along the plate boundary from south to north. EP: Eurasian Plate, PSP: Philippine Sea Plate, TCR: thickened crustal root, FAB: forearc basement. See the detail description in the text.

Range (CER), and north western foothill (NWF) share some consistent feature with low V_p/V_s ratio in shallow depth (0–10 km). This anomalous low V_p/V_s value probably represents the metamorphosed sedimentary rocks (e.g. slate/schist) that contain a high proportion of felsic materials, such as quartz (Christensen, 1996). Alternatively, at such a shallow depth, the crack (i.e. joint) by the exhumation is probably another factor to contribute this low V_p/V_s ratio (Shearer, 1988). For the specific area where Kuo-Chen et al. (2012b) have found the Quartz α - β transition, we also found a local minimum of V_p/V_s ratio deviated from the CER background value at similar depth of 25 km, but it is about 1.68, not as low as 1.55 they obtained. More particularly, the shallow-depth low V_p/V_s ratio in our model is a feature not observed in their study. We have conducted another inversion without the near-surface correction to confirm it a robust feature not caused by the joint inversion with borehole data (Section S.4.1). In this case, the most possible explanation is likely due to the different dataset two studies used. Nonetheless, since almost identical amount and coverage of P- and S-wave data we used, and also the depth is within the good resolution area (Fig. S.4), we conjecture that the absence of this feature in Kuo-Chen et al. (2012b) might result from, first, the active-source experiment can only provide the accurate P- but not the S-wave data for the shallow-structure control, and secondly, the deploying period (2004–2009) of TAIGER stations is too short to record sufficient shallow-depth (<10 km depth) seismicity under Central Range, which are mainly the normal faulting events following the occurrence of 1999 Chi-Chi earthquake.

Moreover, utilizing the V_p/V_s information in 3D, we consistently found a low V_p/V_s block, roughly coincident with moderate-to-high V_p and high V_s , along the plate boundary (dashed circle in Profile AA'–EE', Fig. 6). It seems gradually sinking below the Moho from south to north and always accompanies seismicity (even

in the mantle). The missing of the forearc basement (FAB) between Island and approaching Luzon arc has long been addressed by earlier studies, and seems to be a natural solution for this anomalous block we observed (Fig. 1). Many studies from physical modeling (Chemenda et al., 2001), marine bathymetry mapping (Malavieille et al., 2002), and tomographic images (Cheng, 2009; Shyu et al., 2011) have suggested the FAB had likely subducted eastward under the PSP. However, most of them are the conceptual interpretations. The tomographic delineations of FAB were also restricted to the southernmost LV area so far (Cheng, 2009; Shyu et al., 2011). Here, with resolution-comparable V_p , V_s , and V_p/V_s models, we traced and delineated the FAB northward along entire plate boundary. The FAB, characterized by the moderate-to-high V_p and V_s , and low V_p/V_s ratio, can be identified readily, showing a gradation of fully tectonic subduction under the westernmost edge of PSP. From south of profile BB', this consuming/shortening process was begun from east-dipping thrusting activities, e.g. Chengkung earthquake sequence (Shyu et al., 2011) to west-dipping thrusting activities in profile DD' (Kim et al., 2006). The profile CC' in between clearly shows a transition phase of these two reversal faulting systems (shaded zones) in which the west-dipping faulting develops later above the east-dipping one.

5.4. Subduction-collision complex: a skateboarding edge

The subducted FAB and westernmost edge of PSP can even be traced to further north in profile EE'. Fig. 8 demonstrates a 3-D view of this subduction-collision process by Vs model. The PSP western edge like a skateboarder riding on the FAB (skateboard) all the way subducts northward beneath the EP. The relatively cooled FAB underlying the PSP Moho then serves a brittle mechanism for the shallow double seismic zone observed in profile II' in the man-

tle (shaded area in Fig. 6). The missing of the forearc-basement is rather common in many orogenic belts, but the mechanism has not been clearly pictured yet. Owing to the oblique collision, in eastern Taiwan, we are able to image a gradual process of its missing, in which the forearc-basement is subducted by crossing fault systems and stuffs right under the overriding plate.

Moreover, north of the $\sim 24.5^\circ\text{N}$ latitude, the PSP-western edge seems to start dipping to the west to contact with the Eurasian lithosphere with both west-dipping high velocity zones and earthquake clusters, overlain by a growing corner wedge with low V_s (Fig. 8d and profile EE'). This corner wedge stalled by the Eurasian lithosphere laterally in a 3-D irregular shape may therefore be responsible for the complex shear-wave splitting pattern observed in Okinawa Trough near Taiwan Island (Kuo, B.Y. et al., 2012a).

5.5. Model evaluation by waveform modeling

The recent geodynamic project, TAIGER, aiming at understanding the tectonic process of Taiwan region provides a relatively independent dataset from that of CWBSN for new tomographic models (Kuo-Chen et al., 2012a, 2012b). With an increase of data and different tomographic models, the necessity of a sophisticated means to model evaluation becomes more important than before. Lin et al. (2011) has used first-arrival times from active-source experiment to do so. With known locations of sources, they are able to quantitatively assess the model performance by travel time residuals. However, due to different ray-tracing methods adopted in different studies, e.g. finite difference method (Kim et al., 2005) and pseudo-bending method (Wu et al. 2007, 2009a, 2009b), the finite-difference simulation used in the study of Lin et al. (2011) may not be preferable to all the models. In similar reason, their means of topography correction is also likely to cause potential errors in the assessment due to, again, different parameterization strategies among models.

Nowadays, the technique of numerical simulation, such as spectral-element method (Komatitsch and Tromp, 1999), becomes more and more matured and efficient to applications. By using waveform modeling means, not only travel times but amplitude information can be also naturally considered in evaluation. Fig. 9 shows a simulation example from an earthquake occurred in Hualien area, where is one of the places with highest earthquake frequency in Taiwan. To compare, we also take other two latest models for waveform simulation as well (Wu et al., 2009a; Kuo-Chen et al., 2012a), which are then abbreviated in W09, K12, and H14 (this study) hereinafter. The results performed here are vertical components in three different frequency bands (10–50, 6–60, and 3–50 s, respectively). In the frequency band of 10–50 s, all three models can adequately reproduce the waveforms. The difference, however, appears in shorter frequency bands. The model W09 usually tends to produce larger and more complicated wiggles than the other two, implying that velocity variation/structure in the model W09 tends to over-oscillated/sharp in generating strong scattering waves. The synthetics by model K12 and H14 are also similar in shorter periods, but in the detail, K12 tend to produce more smooth waveforms with stronger first arrivals and weaker later coda. This indicates the model K12 may be slightly over-smooth and therefore generate over-energetic arrivals due to too less smaller-scale heterogeneities for energy scattering. For instance at the station TPUB, compared to the observations, the amplitude of first arrival is obviously over-amplified in synthetics of W09 and K12, but not in H14. This phenomena is even more prominent in 3–50 s frequency band because the small-scale structures take effect (blue shaded zones). In addition to the first arrival, this can also be concluded by the coda characteristics. The coda waves simulated by the model W09 and H14 usually possess more abundant characters than those by the model K12 although

they do not always fit well with observations. The most obvious example may be the station YHNB, at which our model synthetics show more adequate amplitude and long-lasting scattering waves than two others. We then use the following formula to calculate the misfit of waveform fitting, χ , for all three components at high signal-to-noise ratio stations (solid blue triangles in Fig. 9):

$$\chi = \sum_{i=1}^{np} (S(i)_{syn} - S(i)_{obs})^2 / \sum_{i=1}^{np} S(i)_{obs}^2 \quad (7)$$

where $S(i)_{obs}$ and $S(i)_{syn}$ are the synthetic and observational waveforms. np represents the number of sampling points in the time window to compare. Here we used 60 s and it is sufficient long to include most of wave train at stations. In Table 1, the overall results show that the fitting of both K12 and H14 are comparable well, but quantitatively the model H14 has slightly better performance except the N component in longer periods (10–50 and 6–50 s). This is probably due to different dataset from dense arrays across mountain and more careful selection of S_v and S_H arrivals in the model K12 (personal communication). For the model W09 that used a large portion of similar dataset with this study, our better results may result from the elaborate joint inversion (with better data conditioning) and more adequate regularization parameters. The small regularization will produce sharper imaging but with more potential instability in the model. Which can be also demonstrated in Fig. S.7 that the imaging of W09 is always sharper to a bit rugged, but those of K12 is the smoothest on the contrary. Nonetheless, both three models have been good enough for current waveform inversion studies (10–50 s period). This simulation also demonstrates that the waveform-simulation ability of current travel-time tomography such as Kuo-Chen et al. (2012a) and this study can reach a limit period as short as about 5 to 6 second (although more extensive waveform modeling tests are needed). Toward a period as 3 second or shorter, the full-waveform tomography may be a direction to work on.

6. Conclusions

Through an elaborate joint-inversion scheme with augmented S-wave data (equal amount to the P-wave data) and additional S–P time dataset, we can deal with the V_p and the V_s model simultaneously in unified inversion condition and better constrain the source location (linking P- and S-wave, as well as S–P readings together). This then also promises a stable and resolution-comparable V_p/V_s model. By stronger S-wave anomalies and reliable V_p/V_s information, we revisited the subduction-collision orogeny of Taiwan in detail, and propose a “skateboarding edge” model for the westernmost PSP edge that subducts northward by riding atop on the FAB and collides with Eurasian lithosphere to the east in a west-dipping contact beneath the northern Taiwan (Fig. 8). The process of FAB subduction was depicted readily in our images by the mechanism of reversal-faulting shortening along the LV from north to south (Fig. 5, profile BB'–DD'). In the northern LV where the FAB has been fully consumed under below the PSP, it then results in the deep seismic zone in the mantle we observed in profile II' (Fig. 6). Furthermore, plausible melting features are active around the western edge of subducting PSP where is beneath around the Ilan Plain offshore (profile FF' and HH'). Using consistent V_p , V_s , and V_p/V_s model of this study, one can gain more insight into the crustal composition, fluid content, thermodynamical structures, and etc. although here we mainly focused on the tectonic interpretations for subduction-collision complex (and model evaluation). Additionally, the careful near-surface correction by the borehole logging data is first adopted in local earthquake tomography for Taiwan region, improving shallow velocity structures effectively (Fig. 4 and S.6). This correction, by experience, does not

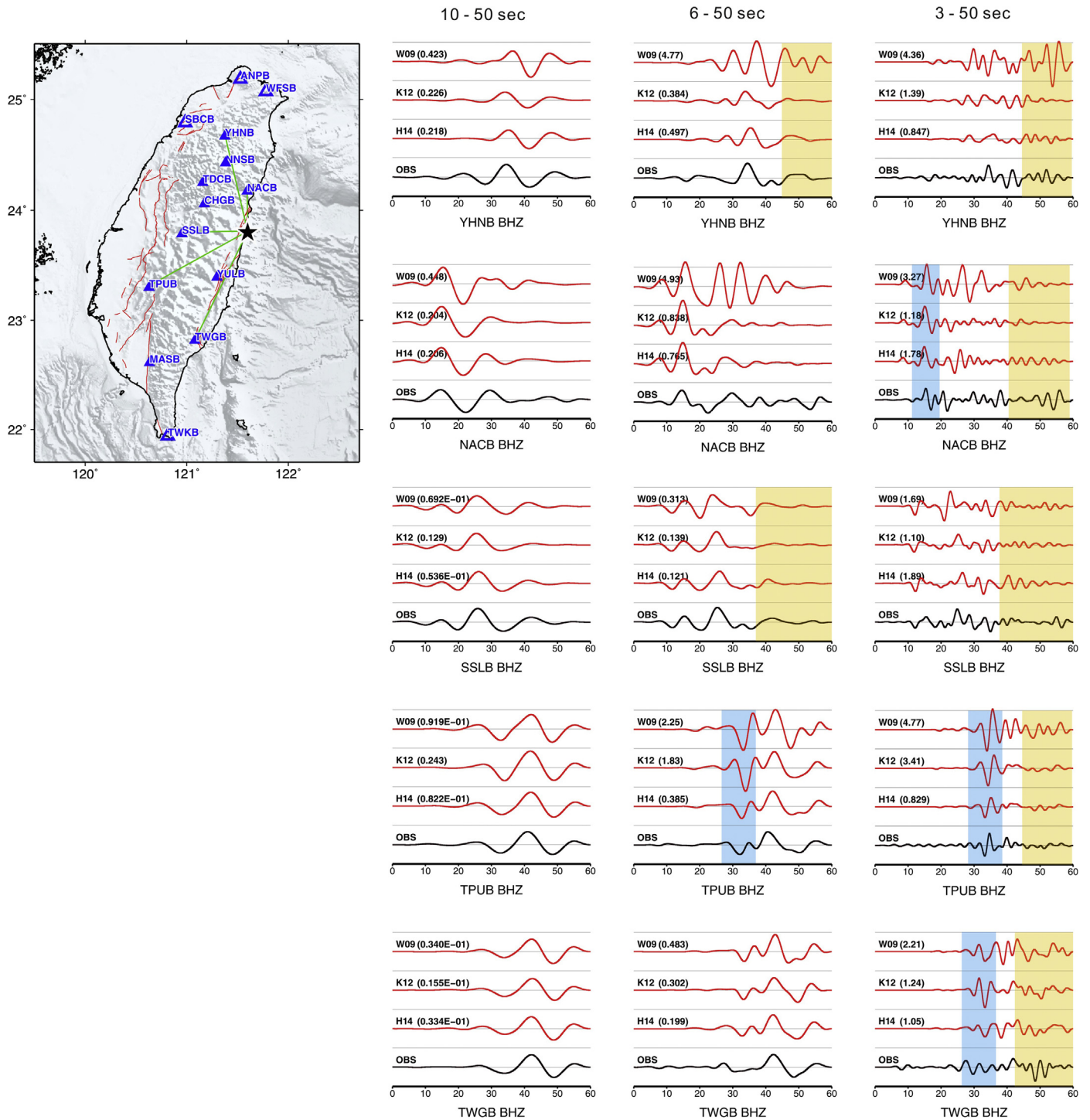


Fig. 9. Model evaluation by waveform modeling in 10–50, 6–50, and 3–50 s frequency band, respectively. The black star represents the source location of simulation. The solid and empty triangles denote the broadband stations with high and low signal-to-noise ratio (SNR), and only high SNR stations are used for waveform fitting calculation in Table 1. The blue and yellow shaded areas roughly mark the first-arrival and coda-wave part of waveforms for discussion in the text.

Table 1

Waveform misfits of H14, K12, and W09 models in different components and frequency bands. The *best fitting model* at each frequency band and component are marked in italic.

Freq. band	10–50 s			6–50 s			3–50 s		
	Model			Model			Model		
Comp.	Z	N	E	Z	N	E	Z	N	E
	H14	<i>0.181</i>	0.573	<i>0.374</i>	<i>0.534</i>	0.992	<i>0.595</i>	<i>1.246</i>	<i>1.405</i>
K12	0.211	<i>0.543</i>	0.421	0.599	<i>0.911</i>	0.624	1.394	1.453	1.107
W09	0.212	0.707	0.549	1.715	1.987	1.405	2.565	3.007	2.052

only effect the most-shallow part of the model but could also calibrate the deep velocity structures in terms of the station correction for travel times. On the other hand, using a waveform modeling approach, the models of this study are evaluated and compared with previous models, showing better waveform fitting in general (Table 1). The results also suggest that the limit of shortest simulation period of current travel-time tomography in Taiwan region is ca. 5 to 6 seconds.

Acknowledgements

Thanks to the Central Weather Bureau, National Center for Research on Earthquake Engineering, TAIGER group, National Central University, and Taiwan Ocean Research Institute kindly providing the data for this integrated work. We are grateful for the constructive discussion with John Suppe, J. Bruce H. Shyu, and H. Kuo-Chen, and very thank two anonymous reviewers who significantly improve and refine the manuscript. This work is supported by the National Science Council, Taiwan.

Appendix A. Supplementary material

Supplementary material related to this article can be found online at <http://dx.doi.org/10.1016/j.epsl.2014.02.026>.

References

- Brocher, T.M., 2005. Empirical relations between elastic wavespeeds and density in the Earth's crust. *Bull. Seismol. Soc. Am.* 95 (6), 2081–2092.
- Chang, H.C., Wu, Y.M., Chen, D.Y., Shin, T.C., Chin, T.L., Chang, W.Y., 2012. An examination of telemetry delay in the central weather bureau seismic network. *Terr. Atmos. Ocean. Sci.* 23 (3), 261–268.
- Chemenda, A.I., Tang, R.K., Stephan, J.F., Konstantinovskaya, E.A., Ivanov, G.M., 2001. New results from physical modeling of arc-continent collision in Taiwan: evolutionary model. *Tectonophysics* 333, 159–178.
- Chen, P.F., Huang, B.S., Liang, W.T., 2004. Evidence of a slab of subducted lithosphere beneath central Taiwan from seismic waveforms and travel times. *Earth Planet. Sci. Lett.* 229, 61–71.
- Cheng, W.B., 2009. Tomographic imaging of the convergent zone in Eastern Taiwan – A subducting forearc sliver revealed? *Tectonophysics* 466, 170–183.
- Chou, H.C., Kuo, B.Y., Chiao, L.Y., Zhao, D., Hung, S.H., 2009. Tomography of the westernmost Ryukyu subduction zone and the serpentinization of the fore-arc mantle. *J. Geophys. Res.* 114, B12301. <http://dx.doi.org/10.1029/2008JB006192>.
- Christensen, N.I., Mooney, W.D., 1995. Seismic velocity structure and composition of the continental crust: A global view. *J. Geophys. Res.* 100 (B7), 9761–9788.
- Christensen, N.I., 1996. Poisson's ratio and crustal seismology. *J. Geophys. Res.* 101 (B2), 3139–3156.
- Cloos, M., Shreve, R.L., 1988. Subduction-channel model of prism accretion, melange formation, sediment subduction, and subduction erosion at convergent plate margins: Part I, background and description. *Pure Appl. Geophys.* 128 (3/4), 455–500.
- Conder, J.A., Wiens, D.A., 2006. Seismic structure beneath the Tonga arc and Lau back-arc basin determined from joint Vp, Vp/Vs tomography. *Geochem. Geophys. Geosyst.* 7 (3), Q03018. <http://dx.doi.org/10.1029/2005GC001113>.
- Eddy, D.R., Van Avendonk, H.J.A., Shillington, D.J., 2013. Compressional and shear-wave velocity structure of the continent-ocean transition zone at the eastern Grand Banks Newfoundland. *Geophys. Res. Lett.* 40, 1–7. <http://dx.doi.org/10.1002/grl.50511>.
- Hacker, B.R., Abers, G.A., Peacock, S.M., 2003. Subduction factory: 1. Theoretical mineralogy, densities, seismic wave speeds, and H₂O contents. *J. Geophys. Res.* 108 (B1), 2029. <http://dx.doi.org/10.1029/2001JB001127>.
- Huang, B.S., Wang, C.Y., Okaya, D., Lee, S.J., Lai, Y.C., Wu, F., Liang, W.T., Huang, W.G., 2013a. Multiple diving waves and steep velocity gradients in the western Taiwan coastal plain: an investigation based on the TAIGER experiment. *Bull. Seismol. Soc. Am.* 103 (2A), 925–935.
- Huang, H.H., Xu, Z.J., Wu, Y.M., Song, X., Huang, B.S., Minh, N.L., 2013b. First local seismic tomography for red river shear zone, northern Vietnam: Stepwise inversion employing crustal P and Pn waves. In: *Special Issue: Active Tectonic Deformation of the Tibetan Plateau and Great Earthquakes*. *Tectonophysics* 584, 230–239.
- Kao, H., Jian, P.R., Ma, K.F., Huang, B.S., Liu, C.C., 1998. Moment-tensor inversion for offshore earthquakes east of Taiwan and their implications to regional collision. *Geophys. Res. Lett.* 25 (19), 3619–3622.
- Kennett, B.L.N., Engdahl, E.R., Buland, R., 1995. Constraints on seismic velocities in the Earth from travel times. *Geophys. J. Int.* 122, 108–112.
- Kennett, B.L.N., Widiyantoro, S., 1998. Joint seismic tomography for bulk sound and shear wave speed in the Earth's mantle. *J. Geophys. Res.* 103 (B6), 12469–12493.
- Kim, K.H., Chiu, J.M., Pujol, J., Chen, K.C., Huang, B.S., Yeh, Y.H., Shen, P., 2005. Three-dimensional V_p and V_s structural models associated with the active subduction and collision tectonics in the Taiwan region. *Geophys. J. Int.* 162, 204–220.
- Kim, K.H., Chiu, J.M., Pujol, J., Chen, K.C., 2006. Polarity reversal of active plate boundary and elevated oceanic upper mantle beneath the collision suture in central eastern Taiwan. *Bull. Seismol. Soc. Am.* 96 (3), 796–806. <http://dx.doi.org/10.1785/0120050106>.
- Kissling, E., Ellsworth, W.L., Eberhart-Phillips, D., Kradolfer, U., 1994. Initial reference models in local earthquake tomography. *J. Geophys. Res.* 99 (B10), 19635–19646.
- Koketsu, K., Sekine, S., 1998. Pseudo-bending method for three-dimensional seismic ray tracing in a spherical earth with discontinuities. *Geophys. J. Int.* 132 (2), 339–346.
- Komatitsch, D., Tromp, J., 1999. Introduction to the spectral-element method for 3-D seismic-wave propagation. *Geophys. J. Int.* 139, 806–822.
- Kuo, B.Y., Wang, C.C., Lin, S.C., Lin, C.R., Chen, P.C., Jang, J.P., Chang, H.K., 2012a. Shear-wave splitting at the edge of the Ryukyu subduction zone. *Earth Planet. Sci. Lett.* 355–356, 262–270.
- Kuo, C.H., Wen, K.L., Hsieh, H.H., Lin, C.M., Chang, T.M., Kuo, K.W., 2012b. Site classification and Vs30 estimation of free-field TSMIP stations using the logging data of EGD. *Eng. Geol.* 129–130, 68–75.
- Kuo-Chen, H., Wu, F.T., Roecker, S.W., 2012a. Three-dimensional P velocity structures of the lithosphere beneath Taiwan from the analysis of TAIGER and related seismic data sets. *J. Geophys. Res.* 117, B06306. <http://dx.doi.org/10.1029/2011JB009108>.
- Kuo-Chen, H., Wu, F.T., Jenkins, D.M., Mechie, J., Roecker, S.W., Wang, C.Y., Huang, B.S., 2012b. Seismic evidence for the a-b quartz transition beneath Taiwan from Vp/Vs tomography. *Geophys. Res. Lett.* 39, L22302. <http://dx.doi.org/10.1029/2012GL053649>.
- Lee, S.J., Ma, K.F., Chen, H.W., 2006. Three dimensional dense strong motion waveform inversion for the rupture process of the 1999 Chi-Chi, Taiwan, earthquake. *J. Geophys. Res.* 111, B11308. <http://dx.doi.org/10.1029/2005JB004097>.
- Lee, S.J., Chen, H.W., Liu, Q., Komatitsch, D., Huang, B.S., Tromp, J., 2008. Three-dimensional simulations of seismic wave propagation in the Taipei basin with realistic topography based upon the spectral-element method. *Bull. Seismol. Soc. Am.* 98, 253–264. <http://dx.doi.org/10.1785/0120070033>.
- Lees, J.M., Crosson, R.S., 1989. Tomographic inversion for three-dimensional velocity structure at Mount St. Helens using earthquake data. *J. Geophys. Res.* 94, 5716–5728.
- Leveque, J.J., Rivera, L., Wittlinger, G., 1993. On the use of the checker-board test to assess the resolution of tomographic inversions. *Geophys. J. Int.* 115, 313–318.
- Liang, C., Song, X., Huang, J., 2004. Tomographic inversion of Pn travel times in China. *J. Geophys. Res.* 109, B11304. <http://dx.doi.org/10.1029/2003JB002789>.
- Liao, Y.C., Hsu, S.K., Chang, C.H., Doo, W.B., Ho, M.Y., Lo, C.L., Lee, C.S., 2008. Seismic tomography off SW Taiwan: A joint inversion from OBS and onshore data of 2006 Pingtung aftershocks. *Terr. Atmos. Ocean. Sci.* 19 (6), 729–741.
- Lin, A.T., Watts, A.B., Hesselbo, S.P., 2003. Cenozoic stratigraphy and subsidence history of the South China Seamargin in the Taiwan region. *Basin Res.* <http://dx.doi.org/10.1046/j.1365-2117.2003.00215.x>.
- Lin, C.H., 2009. Compelling evidence of an aseismic slab beneath central Taiwan from a dense linear seismic array. *Tectonophysics* 466, 205–212.
- Lin, J.Y., Hsu, S.K., Sibuet, J.C., 2004. Melting features along the western Ryukyu slab edge (northeast Taiwan): tomographic evidence. *J. Geophys. Res.* 109, B12402. <http://dx.doi.org/10.1029/2004JB003260>.
- Liu, T.K., Hsieh, S., Chen, Y.G., Chen, W.S., 2001. Thermo-Kinematic evolution of the Taiwan oblique-collision mountain belt as revealed by zircon fission track dating. *Earth Planet. Sci. Lett.* 186, 45–56.
- Lin, Y.P., Zhao, L., Hung, S.H., 2011. Assessment of tomography models of Taiwan using first-arrival times from the TAIGER active-source experiment. *Bull. Seismol. Soc. Am.* 101 (2), 866–880.
- Ma, K.F., Wang, J.H., Zhao, D., 1996. Three-dimensional seismic velocity structure of the crust and uppermost mantle beneath Taiwan. *J. Phys. Earth* 44, 85–105.
- Malavieille, J., Lallemand, S.E., Dominguez, S., Deschamps, A., 2002. Arc-Continent collision in Taiwan: New marine observations and tectonic evolution. *Spec. Pap., Geol. Soc. Am.* 358, 187–211.
- Rau, R.J., Wu, F.T., 1995. Tomographic imaging of lithospheric structures under Taiwan. *Earth Planet. Sci. Lett.* 133, 517–532.
- Roecker, S.W., Yeh, Y.H., Tsai, Y.B., 1987. Three-dimensional P and S wave velocity structures beneath Taiwan: Deep structure beneath an arc-continent collision. *J. Geophys. Res.* 92, 10547–10570.
- Roecker, S., Thurber, C., Roberts, K., Powell, L., 2006. Refining the image of the San Andreas Fault near Parkfield, California using a finite difference travel time computation technique. *Tectonophysics* 426, 189–205.
- Romanowicz, B., 2003. Global mantle tomography: progress status in the past 10 years. *Annu. Rev. Earth Planet. Sci.* 31, 303–328.
- Schutt, D.L., Humphreys, E.D., 2004. P and S wave velocity and VP/VS in the wake of the Yellowstone hot spot. *J. Geophys. Res.* 109, B01305. <http://dx.doi.org/10.1029/2003JB002442>.
- Shearer, P., 1988. Cracked media, Poisson's ratio and the structure of the upper oceanic crust. *Geophys. J.* 92, 357–362.

- Shin, T.C., 1992. Some implications of Taiwan tectonic features from the data collected by the Central Weather Bureau Seismic Network. *Meteorol. Bull.* 38, 23–48 (in Chinese).
- Shin, T.C., 1993. Progress summary of the Taiwan strong motion instrumentation program. In: *Proceeding of Symposium on Taiwan Strong Motion Instrumentation Program*. Central Weather Bureau, Taipei, Taiwan, pp. 1–10 (in Chinese).
- Shin, T.C., Teng, T.L., 2001. An Overview of the 1999 Chi-Chi, Taiwan, Earthquake. *Bull. Seismol. Soc. Am.* 91 (5), 895–913.
- Shin, T.C., Tsai, Y.B., Yeh, Y.T., Liu, C.C., Wu, Y.M., 2003. Strong motion instrumentation programs in Taiwan. In: Lee, W.H.K., Kanamori, H., Jennings, P.C. (Eds.), *Handbook of Earthquake and Engineering Seismology*. Academic Press, New York, pp. 1057–1602.
- Shyu, J.B.H., Wu, Y.M., Chang, C.H., Huang, H.H., 2011. Tectonic erosion and the removal of forearc lithosphere during arc-continent collision: Evidence from recent earthquake sequences and tomography results in eastern Taiwan. *J. Asian Earth Sci.* 42, 415–422.
- Suppe, J., 1981. Mechanics of mountain building and metamorphism in Taiwan. *Mem. Geol. Soc. China* 4, 67–89.
- Suppe, J., 1984. Kinematics of arc-continent collision, flipping of subduction, and back-arc spreading near Taiwan. *Mem. Geol. Soc. China* 6, 21–33.
- Tellez, J., Cordoba, D., 1998. Crustal shear-wave velocity and poisson's ratio distribution in northwest Spain. *J. Geodyn.* 25 (1), 35–45.
- Teng, L.S., 1990. Geotectonic evolution of late Cenozoic arc-continent collision in Taiwan. *Tectonophysics* 183, 57–76.
- Thurber, C.H., 1992. Hypocenter-velocity structure coupling in local earthquake tomography. *Phys. Earth Planet. Inter.* 75, 55–62.
- Thurber, C.H., Eberhart-Phillips, D., 1999. Local earthquake tomography with flexible gridding. *Comput. Geosci.* 25, 809–818.
- Um, J., Thurber, C., 1987. A fast algorithm for two-point seismic ray tracing. *Bull. Seismol. Soc. Am.* 77 (3), 972–986.
- Ustaszewski, K., Wu, Y.M., Suppe, J., Huang, H.H., Chang, C.H., Carena, S., 2012. Crust-mantle boundaries in the Taiwan – Luzon arc-continent collision system determined from local earthquake tomography and 1D models: Implications for the mode of subduction polarity reversal. In: *Special Issue: Geodynamics and Environment in East Asia*. *Tectonophysics* 578, 31–49.
- Walck, M.C., 1988. Three-dimensional V_P/V_S variations for the Coso Region, California. *J. Geophys. Res.* 93 (B3), 2047–2052.
- Wang, Z., Zhao, D., Wang, J., Kao, H., 2006. Tomographic evidence for the Eurasian lithosphere subducting beneath south Taiwan. *Geophys. Res. Lett.* 33, L18306. <http://dx.doi.org/10.1029/2006GL027166>.
- Wang, Z., Fukao, Y., Zhao, D., Kodaira, S., Mishra, O.P., Yamada, A., 2009. Structural heterogeneities in the crust and upper mantle beneath Taiwan. *Tectonophysics* 476, 460–477. <http://dx.doi.org/10.1016/j.tecto.2009.07.018>.
- Wu, F.T., Rau, R.J., Salzberg, D., 1997. Taiwan orogeny: thin-skinned or lithospheric collision? *Tectonophysics* 274, 191–220.
- Wu, Y.M., Chang, C.H., Zhao, L., Shyu, J.B.H., Chen, Y.G., Sieh, K., Avouac, J.P., 2007. Seismic tomography of Taiwan: Improved constraints from a dense network of strong motion stations. *J. Geophys. Res.* 112, B08312. <http://dx.doi.org/10.1029/2007JB004983>.
- Wu, Y.M., Chang, C.H., Zhao, L., Teng, T.L., Nakamura, M., 2008. A comprehensive relocation of earthquakes in Taiwan from 1991 to 2005. *Bull. Seismol. Soc. Am.* 98, 1471–1481. <http://dx.doi.org/10.1785/0120070166>.
- Wu, Y.M., Shyu, J.B.H., Chang, C.H., Zhao, L., Nakamura, M., Hsu, S.K., 2009a. Improved seismic tomography offshore northeastern Taiwan: implications for subduction and collision processes between Taiwan and the southernmost Ryukyu. *Geophys. J. Int.* 178, 1042–1054.
- Wu, Y.M., Chang, C.H., Zhao, L., Hsiao, N.C., Chen, Y.G., Hsu, S.K., 2009b. Relocation of the 2006 Pingtung earthquake sequence and seismotectonics in Southern Taiwan. *Tectonophysics* 479, 19–27. <http://dx.doi.org/10.1016/j.tecto.2008.12.001>.
- Xu, Z.J., Song, X., 2010. Joint inversion for crustal and Pn velocities and Moho depth in Eastern Margin of the Tibetan Plateau. *Tectonophysics* 491, 185–193.
- Yu, S.B., Chen, H.Y., Kuo, L.C., 1997. Velocity field of GPS stations in the Taiwan area. *Tectonophysics* 274, 41–59.
- Zelt, C.A., 1998. Lateral velocity resolution from three-dimensional seismic refraction data. *Geophys. J. Int.* 135, 1101–1112.
- Zhang, X., Brown, D., Deng, Y., 2011. Crustal composition model across the Bangong–Nujiang suture belt derived from INDEPTH III velocity data. *J. Geophys. Eng.* 8, 549–559.